Atomic XAFS as a Probe of Electron Transfer within Organometallic Complexes: Data analysis and Theoretical Calculations

6 AUTHORS, INCLUDING:

Moniek Tromp
University of Amsterdam
61 PUBLICATIONS **927** CITATIONS

Bert Klein Gebbink
Utrecht University
237 PUBLICATIONS **4,188** CITATIONS

Gerard van koten
Utrecht University
1,113 PUBLICATIONS **27,997** CITATIONS

D.C. Koningsberger
Utrecht University
284 PUBLICATIONS **8,594** CITATIONS

Atomic XAFS as a probe of electron transfer within organometallic complexes: Data analysis and theoretical calculations

Moniek Tromp,[a] Martijn Q. Slagt,[b] Robertus J. M. Klein Gebbink,[b] Gerard van Koten,[b] David E. Ramaker[c] and Diek C. Koningsberger*[a]

[a] Debye Institute, Dept. Inorganic Chemistry and Catalysis, Utrecht University, P.O. Box 80083, Utrecht, 3508 TB, The Netherlands. E-mail: D.C.Koningsberger@chem.uu.nl; Fax: +31 30 251 1027; Tel: +31 30 253 7400
[b] Debye Institute, Dept. Metal-Mediated Synthesis, Utrecht University, Padualaan 8, Utrecht, 3584 CH, The Netherlands
[c] Dept. Chemistry and Materials Science Institute, George Washington University, Washington, DC 20052, USA

The atomic XAFS (AXAFS) contributions in the Pt $L_{2,3}$ X-ray absorption fine structure spectra (XAFS) of [PtCl(NCN)-Z] pincer complexes are shown to be a sensitive probe of changes in the electron density on the Pt atom induced by changes in a *para*-substituent on the neighboring benzene ring. Such electron density information is similar yet complementary to NMR data. These complexes provide a unique system for examining inductive effects on the AXAFS data, since the geometry around the Pt atom remains unchanged. An initial brief report on this work has been given previously. In this paper a more complete description of the AXAFS isolation technique and theoretical interpretation is given. The isolation of the AXAFS contributions from the XAFS spectrum is extensively described. The dependence of the AXAFS shape and intensity on the Pt atom electron density are shown and discussed in detail.

Introduction

Transition metal complexes with NCN-pincer ligands (NCN = $[2,6-(Me_2NCH_2)_2C_6H_3]^-$) have been prepared for numerous applications in the fields of catalysis, catalyst immobilization, supramolecular assembly, and sensor materials.[1] The introduction of substituents at the *para*-position of the pincer ligand benzene ring allows one to tune the metal center electronically. This functionalization has been most successful with pincer complexes from the nickel triad (Ni, Pd, Pt), due to their exceptional stability. The electronic tuning of pincer complexes has been shown to be a very powerful tool for tuning the reactivity of the catalytically active pincers, *e.g.* NCN-pincer nickel complexes used for the Karasch addition. *para*-Substituents which donate electrons decrease the oxidation potential of the Ni(II)/Ni(III) couple, resulting in more active atom transfer catalysts.[2]

Recently we have been able to synthesize a library of *para*-substituted NCN-pincer platinum complexes [PtCl(NCN-Z)] to study the influence of the substituent on the electronic properties of the metal centre.[3] It would be very useful to be able to determine the electron density of the pincers directly. In the case of [PtCl(NCN-Z)] pincer complexes, this has been shown to be possible using [195]Pt NMR.[3b] However, NMR can only be applied to a limited amount of atoms and thus other techniques need to be explored. Recently, we have developed a new technique, which directly provides information about the electronic structure of the metal under investigation, so-called Atomic X-ray Absorption Fine Structure Spectroscopy (AXAFS). So far, AXAFS has been demonstrated for mainly electrochemical systems and heterogeneous catalysts[4,5] in which both geometric and electronic effects simultaneously influence the AXAFS signal. This complicates the analysis and interpretation.

In this study the above described [PtCl(NCN-Z)] pincer complexes are used as model complexes to validate the AXAFS technique and to verify the AXAFS theoretical interpretation. The electronic properties of the Pt pincer complexes can be tuned selectively *via* the *para*-substituent. The geometry of the coordination environment of the platinum nucleus stays nearly unchanged upon *para*-substitution; consequently, changes in the electron density of the Pt pincer complexes arising from factors other than the *para*-substitution can be neglected. This makes the Pt pincer system perfect for extensively demonstrating and proving the AXAFS theory. An initial brief report on these AXAFS results has been given in ref. 6. This paper gives an in-depth study in which the data-analysis, AXAFS isolation and the different electronic effects on the AXAFS intensity and shape are extensively discussed. Moreover, the strength of the AXAFS technique for the direct electron density determination is shown.

Experimental

Synthesis [PtCl(NCN-Z)] pincers

The [PtCl(NCN-Z)] pincers were synthesized as described in the literature with a series of different *para*-substituents, *i.e.* from substituents with electron withdrawing (Z = COOH) to electron donating properties (Z = NH$_2$) and a neutral substituent H.[3]

Pt L_2 and L_3 edge XAFS

Pt L_2 and L_3-edge (respectively 11564 and 13272 eV) EXAFS spectra were measured at the Hamburger Synchrotronstrahlungslabor

(Hasylab), Germany, on Beamline X1, using a Si(311) double crystal monochromator. The monochromator was detuned to 50% intensity to avoid effects of higher harmonics. The measurements were done in the transmission mode using optimized ion chambers as detectors. To decrease noise, three scans were collected for each sample and averaged.

Both Pt L_2 and L_3 edge XAFS data were collected on the solid samples at liquid nitrogen temperature. Solid material and a known amount of boron nitride were thoroughly mixed and pressed into a self-supporting wafer (calculated to have a maximum total absorbance of 2.5 with a preferable step-size of 1) and placed in an air- and water-tight EXAFS cell provided with X-ray transparent beryllium windows.[7]

Theory and background subtraction

AXAFS

X-ray absorption fine structure (XAFS) spectroscopy is a technique based on the photoelectric effect. After absorption of an X-ray photon, a core electron is ejected to the continuum. This photoelectron can be described by a spherical wave, which travels outward and interacts with its surroundings. For extended XAFS (EXAFS) the outgoing electron scatters against the potential (electron clouds) of neighboring atoms (Fig. 1), creating a backscattered wave that interferes with the outgoing photoelectron wave. The resultant EXAFS data give information about the geometry around the absorber atom.

The total X-ray absorption $\mu(k)$ is normally defined as $\mu(k) = \mu_0(k) (1 + \chi_{EX})$, with χ_{EX} the EXAFS function and $\mu_0(k)$ the atomic X-ray absorption coefficient, or atomic background. Conventionally, this atomic background was assumed to be smooth and non-oscillatory. However, several authors[8–10] have shown in the past few years that this does not have to be true since the atomic X-ray absorption coefficient can have structure due to scattering of the photoelectron against the potential determined by the electron cloud of the atom from which the photoelectron is excited. Therefore this structure is called atomic XAFS (AXAFS). The atomic absorption coefficient can thus be written as $\mu_0(k) = \mu_{FREE}(1 + \chi_{AX})$, with χ_{AX} the AXAFS fine structure and μ_{FREE} the free atomic background.[8,11]

AXAFS represents the change in scattering by the embedded absorber atom relative to the free absorber atom (Fig. 1). This change is due to bonding of the absorbing atom with its environment and thus gives information about the electronic structure of the absorber atom. Consequently, any change in the environment altering the electronic structure of the absorbing atom, should be reflected in the AXAFS.

In Fig. 2, AXAFS is schematically described using the well-known muffin-tin approximation,[10,12] which is a good method to approximate the embedded atom potential. The interstitial potential V_{int} determines the zero energy of the system.[11] The free atom potential U_{free} reflects the electron distribution in the
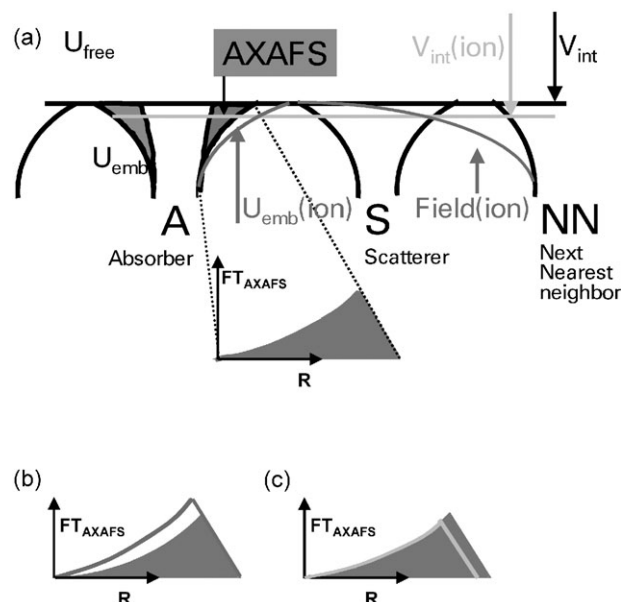
Fig. 2 Schematic physical potential model, based on the muffin tin approximation, defining AXAFS as the dark grey area. (a) Changing AXAFS intensity and shape (dark and light grey lines) due to exclusively (b) space field effect (dark grey lines) or (c) bond inductive effect (light grey lines) from change in the NN (*i.e.*, in this work change in *para* substituent).

free atom, whereas the embedded potential U_{emb} reflects the electron distribution after embedding the free atom into its chemical environment and allowing interaction with neighbors (note potentials which are functions of R are denoted with U, constants with V). The AXAFS is best reflected in the Fourier Transform (FT) of the χ_{AX} producing the first peak at approximately 1/2 the first shell bond length. The FT of AXAFS is then shown to be directly proportional to $U_{emb}(R) - U_{free}(R)$ and therefore its shape and intensity directly reflect electronic and chemical bonding information.[11]

Two effects distinguished with AXAFS

Due to polarization of the absorbing atom by its neighbors, two important effects on the electronic properties can be distinguished with AXAFS: (a) the Coulomb field effect, *i.e.* the effect induced by a Coulomb field, correlated to different charges on neighboring substituents (thereby altering the "roll over" of the interatomic potential, dark grey lines in Figs. 2a and b) and (b) the bond inductive effect, induced by a difference in electronegativity of the substituent (thereby altering the value of V_{int}, light grey lines in Figs. 2a and c). For an isolated Coulomb field effect as shown in Fig. 2a (dark grey), the AXAFS intensity increases and a simultaneous shift to lower radius is observed (Fig. 2b). For the isolated bond inductive effect as shown in Fig. 2a (light grey), the intensity goes down with a simultaneous shift to lower distance (Fig. 2c). Moreover, the difference in AXAFS shape change illustrated is typical for the two different effects ('lower R part' increased by field effect *vs.* 'higher R part' decreased by inductive effect).

From a more chemical viewpoint, and specifically applied to the Pt-pincers described in this study, the two effects can be described as follows. The placement of a more electronegative element Z (Scheme 1) creates an inductive effect on the benzene ring. In Scheme 1a the inductive effect stops at the benzene ring, leaving positive charges at the carbon atoms near Pt. This creates a Coulomb field change on the Pt, which shifts the valence orbitals to higher binding energy, thereby increasing the AXAFS (Fig. 2b). In contrast, if the inductive effect proceeds all the way to the Pt (Scheme 1b), the reduced electron density near the Fermi level or HOMO decreases the
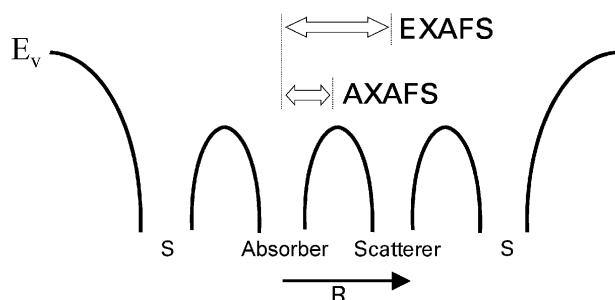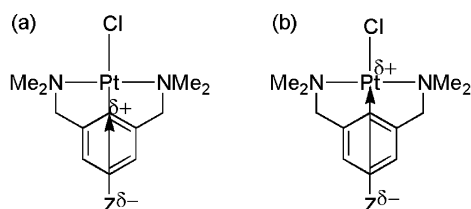

E_v — EXAFS — AXAFS

Fig. 1 Physical origin of EXAFS and AXAFS in a schematic potential model, with A = absorber, B = scatterer, E_v = vacuum level, R = distance.

Scheme 1 *para*-Substituted NCN-pincer platinum complexes. Z creates an inductive effect on (a) the benzene ring or (b) the Pt atom.

Table 1 FEFF8 input parameters used for the calculations of phase shifts and backscattering amplitudes

Atom pair	$\sigma^2/\text{Å}^2$	S_0^2	V_r/eV	V_i/eV	Potential
Pt–Cl	0.0023	0.67	5.5	3.0	Dirac–Hara
Pt–C/N	0.0020	0.93	10.4	3.0	Hedin–Lundquist

Table 2 Best fit results for the experimental data using the theoretical references, including fitting parameters. Fits were performed in *R*-space, k^3-weighted

Shell	N	R/Å	$\Delta\sigma^2/\text{Å}^2$	E_0/eV	$\Delta k/\text{Å}^{-1}$	ΔR/Å
Pt–Cl	6.1	2.31	0.00001	−0.06	3.6–14.0	1.6–2.3
Pt–C/N	3.9	1.98	0.00001	0.02	2.5–12.9	1.0–2.0

AXAFS (Fig. 2c). Therefore, the relative change in the AXAFS directly reflects the response of the absorber atom to the placement of that substituent in the molecule.

Resonance effects can also play a role in these [PtCl(NCN-Z)] pincer complexes, especially for complexes with substituents with a lone pair of electrons. AXAFS however will not be able to distinguish between inductive and resonance effects since both result in a similar electron density change on the Pt atom. Moreover, the resonance effects in the Pt complexes described in this study are not expected to play a big role, since the Pt–C and Pt–Cl distances are the same for all complexes (*vide infra*). Here, we will thus only distinguish between Coulomb and inductive effects.

Background subtraction

Isolation of the AXAFS contribution from the XAS data requires a very careful background subtraction procedure. As recognized in the literature, this background subtraction procedure is not straightforward.[10–13] First the pre-edge background, which is approximated by a modified Victoreen curve,[14] is subtracted after which the edge position is chosen.[15] The post-edge background is approximated by a normal cubic-spline function.[15,16] The background subtraction procedure is extensively described in the literature.[10] Detailed criteria are given how to optimize both the AXAFS χ_{AX} and EXAFS χ_{EX} contributions in the resulting XAFS data, and how to separate double electron excitations (DEE) and the Ramsauer–Townsend resonances (RTR) that are present in the free atom contribution from the oscillatory part of the spectrum. In order to perform a careful DEE/AXAFS/EXAFS separation, it is important to have the ability to use a continuous adjustable smooth parameter. The importance of this capability will be shown in this study.

The criteria for background removal were defined previously as follows:[10,11]

(a) In the FT diminish the contribution at $R < 0.5$ Å, *i.e.* the DEE and RTR, as much as possible. Check whether the DEE and RTR fully remain in the background by examining the background.

(b) Make sure the EXAFS intensity is unchanged (unreduced).

(c) Check both k^1- and k^3-weighted spectra, for different k-ranges, including low k-values.

These criteria can be applied generally. However, they were constructed for XAFS data of samples in which the AXAFS and the EXAFS peaks in the Fourier transform of the XAFS data have less or no overlap. For these cases, applying these criteria is easy and straightforward. For the [PtCl(NCN-Z)] pincer complexes studied in this paper, we will see that the criteria are much more difficult to apply due to tailing of the EXAFS first shell contribution down to 0 Å and consequently severely overlapping with the AXAFS (*vide infra*).

EXAFS data analysis

For the EXAFS data-analysis the commercially available program XDAP[17] was used. Theoretical data for phase shifts

and backscattering amplitudes were generated using the FEFF8 code.[18] EXAFS data from reference compounds were used to calibrate the theoretical references: H_2PtCl_6 for Pt-Cl, and $Rb_2Pt(CN)_4(1.5\ H_2O)$ for both Pt-C and Pt-N since C and N are neighboring atoms in the periodic table. The theoretical references were optimized as described by Koningsberger *et al.*[19] Table 1 gives the FEFF8 input parameters. V_i is estimated to be 3 eV. S_0^2, the Debye–Waller factor and V_r were varied until the generated references produce an optimal fit in *R*-space of the first coordination shell of the Fourier transform of the experimental EXAFS spectra of the above mentioned reference compounds (see Table 2).

These calibrated references could be used to fit the EXAFS data of the pincer samples down to very low values of k ($k \geq 2.5$ Å^{-1}). During *R*-space fitting of the EXAFS data, the difference file technique was used to judge whether for all applied k weightings a good analysis for all contributions was obtained.[20]

FEFF8 calculations[18]

The FEFF8 code[18] was used to perform *ab-initio* self-consistent field, real-space, full multiple scattering calculations.[21] FEFF8 implements self-consistent field potentials for the determination of the Fermi-level and the charge transfer. The calculations were performed using the Hedin–Lundquist exchange correlation potential. A core-hole is included on the absorber atom in order to mimic the final state of the photon absorption process. The full crystal structures are used as input for the FEFF8 calculations. The self-consistent field (SCF) radius was chosen to be slightly longer than the longest Pt-neighbor distance in the complex (*i.e.* $R_{SCF} = 6.7$ Å for the [PtCl(NCN-NH$_2$)] pincer complex, $R_{SCF} = 5.9$ Å for the [PtCl(NCN-H)] pincer complex, $R_{SCF} = 7.9$ Å for the [PtCl(NCN-COOH)] pincer complex). The experimental broadening V_i was chosen at 3 eV, similar to that used for the calibrated references. S_0^2 was chosen at 1.0 for all complexes.

X-ray absorption near edge spectra (XANES) are simulated using a full multiple scattering (FMS) with $R_{FMS} = R_{SCF}$. The FMS was not used for the EXAFS/AXAFS calculations since implementation of this card results in large inaccuracies in the calculated EXAFS data at high energy.

Results

XANES

The normalized raw XAFS Pt L_2- and Pt L_3-edge data obtained for the series of [PtCl(NCN-Z)] complexes are shown in Fig. 3. Changes in the edge position and features in the XANES region are barely visible. Very small double peaks
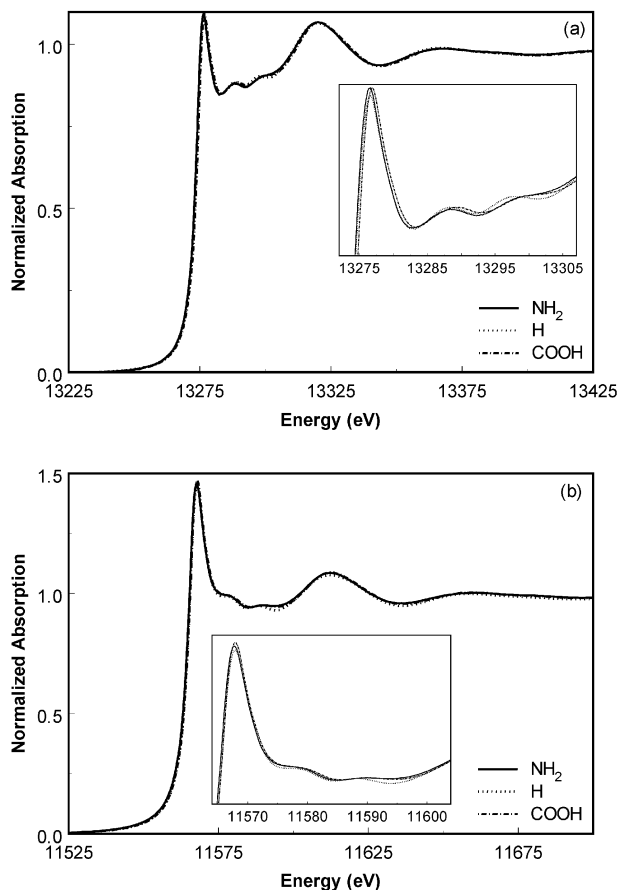
Fig. 3 Normalized experimental XAS data of [PtCl(NCN-Z)] pincers (a) Pt L_2-edge, (b) Pt L_3-edge.

are present just above the whiteline in both the Pt L_2- and L_3-edge data.

Background subtraction

A careful background subtraction is performed, optimizing the AXAFS and EXAFS contributions in the XAFS data and simultaneously leaving the double electron excitations in the background as described in the literature.[22] However, this background subtraction procedure was described previously for samples in which the first shell contribution is clearly separated from the AXAFS. Moreover, for the [PtCl(NCN-Z)] pincer complexes described here only one Pt(II) atom is present, in contrast to the larger Pt(0) clusters described in the previous studies. The C and N atoms are located close to the Pt, *i.e.* around 1.8 and 2.1 Å.[3] Consequently, the EXAFS contributions tail to R distances below 1 Å causing interference with the AXAFS peak. This can even result in reduction of the AXAFS peak amplitude in the FT of the raw data.

Figs. 4a and b show respectively the k^1-weighted and k^3-weighted FT data after background subtraction with different smoothing parameters (SM). Especially in the k^1-weighted case, it is clear that the EXAFS is tailing to small R distance and is severely overlapping with the DEE and AXAFS contributions (see also Fig. 8 later). The assignment of the different contributions is based upon the results presented in an earlier study.[22] Thus the FT's should be very carefully examined in order to determine a reliable background. Fig. 4a shows that with increasing SM the intensity of the AXAFS/EXAFS peak at $\sim$0.9 Å and the higher EXAFS peaks are increasing (first shell contribution peaking around 1.4 Å, *vide infra*). For a SM of 3.75 the EXAFS peaks shift somewhat to higher R and a small peak around 0.2 Å is formed. When the SM is even more increased to 4.00, large peaks at low R are now formed, clearly

corresponding to DEE. Simultaneously, the EXAFS peaks now significantly shift to longer distances.

The k^3-weighted FT's displayed in Fig. 4b, show similar trends. All peaks increase with increasing SM. From SM = 3.75, the increase of peak intensity is accompanied by a significant increase of the contribution at $R < 0.5$ Å. Moreover, the positions of the peaks between 0.5 and 2.0 Å shift to higher distances. For SM = 4.00, the DEE contribution below 0.5 Å is large, moreover, all other contributions (peaks) have significantly shifted position.

Examination of the corresponding backgrounds in Fig. 5 with the same SM values as displayed in Fig. 4, show that for SM < 3.75 the step-like DEE feature with the usual onset at $\sim$140 eV is visible,[10] whereas for SM parameters of 3.75 and above, the background flattens and the DEE is diminished.

Based on the FT's and corresponding backgrounds, a background with SM = 3.50 is chosen here as optimal. For a correct background subtraction, the DEE are required to be left in the background. This is true for backgrounds with SM < 3.75 (Fig. 4). Simultaneously, in the resulting FT, the contribution of DEE/RTR should be diminished as much as possible. In Figs. 4a and b, this happens for SM < 3.75. Optimization of both the AXAFS and EXAFS contributions in all different k-weightings using the criteria as mentioned above then results in an optimal background with SM = 3.50 (solid line) for the [PtCl(NCN-H)] pincer complex shown here.

It is always possible that the final choice of the SM parameter does not lead to an optimal separation between the DEE, AXAFS and EXAFS. However, it should be noted that even without an optimal background subtraction, identical trends in the final AXAFS data are still found as long as the background is performed consistently. The final trend in the AXAFS data is the same even though the absolute AXAFS areas may be different. Further, the AXAFS signal obtained is also
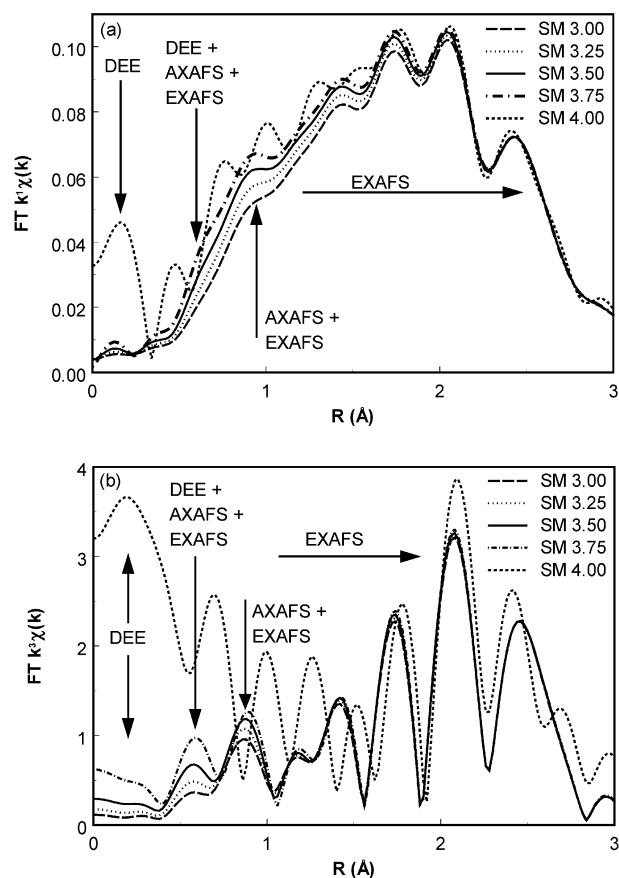

Fig. 4 Fourier Transforms (k^1, Δk = 1.6–15 Å^{-1}) of the [PtCl(NCN-H)] pincer XAFS data for different smoothing parameters SM (a) k^1-weighted, (b) k^3-weighted.
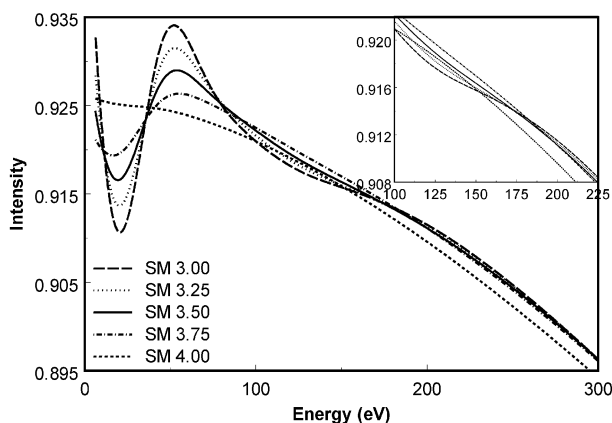
Fig. 5 Background of [PtCl-(NCN)-H] pincer XAFS data as a function of the smoothing parameter (SM).

somewhat dependent on a careful EXAFS analysis since the final choice of the EXAFS parameters of the overlapping shells at low R (overlapping with the AXAFS) easily influences the resulting AXAFS data.

After background subtraction, the absorption data are normalized at 50 eV after the absorption edge and the final $\chi(k)$ is calculated.[15] All pincer complex XAFS data were treated as described above.

EXAFS analysis

The final EXAFS data of the three [PtCl(NCN-Z)] pincer complexes are shown in Fig. 6a. The data are of excellent quality with a very high signal/noise ratio. The noise level can be determined to be ∼0.0002 in the high k-range in the
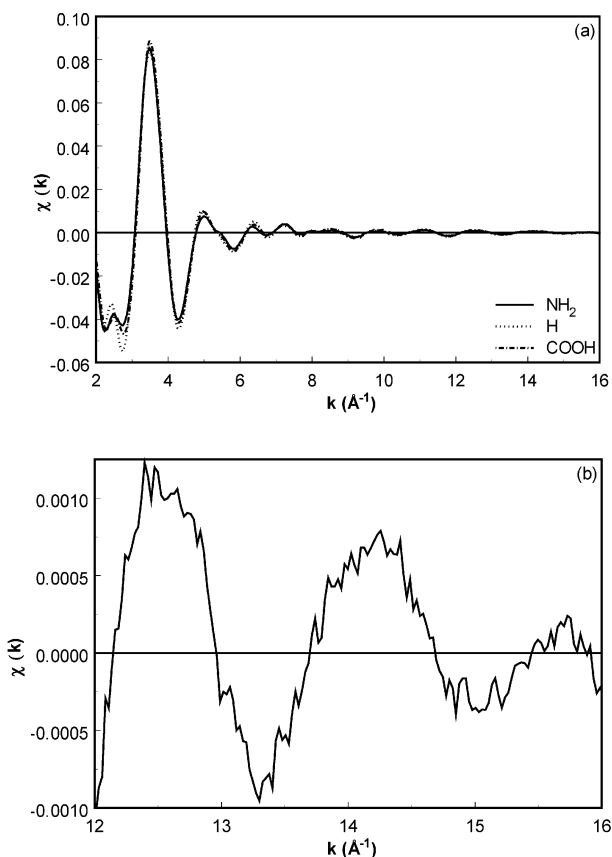

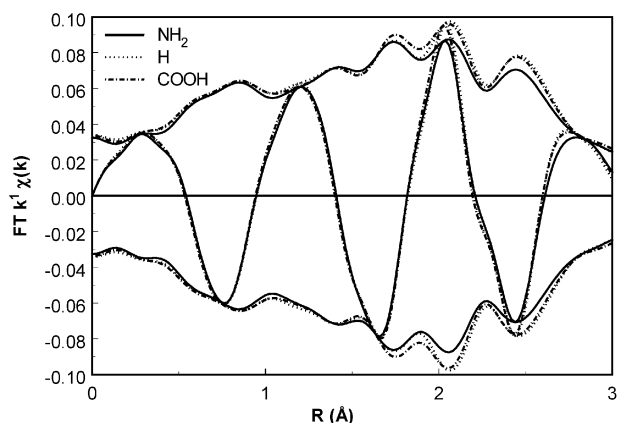**Fig. 7** Fourier Transforms (k^1-weighted) of EXAFS data of the [PtCl(NCN-Z)] pincer complexes, for Z = NH$_2$ (solid line), Z = H (striped line), Z = COOH (dotted line).

enlargement in Fig. 6b. Only small changes in the intensity of the final EXAFS data at low values of k can be observed for the different samples. In the corresponding FT's shown in Fig. 7, these small changes are visible as small intensity changes over the R-range shown here, whereas the imaginary parts are similar for all complexes.

The difference file technique was used to judge whether a good analysis for all Pt-X contributions in all weightings was achieved.[19,20] A good fit can be concluded from Fig. 8 showing the raw data and fit for different k-weightings and from the corresponding low variances in the fit parameters given in Table 3. Moreover, during the fitting procedure the difference files were examined carefully. In Fig. 9 the k^1-weighted difference files and fits for the single shell contributions are shown,
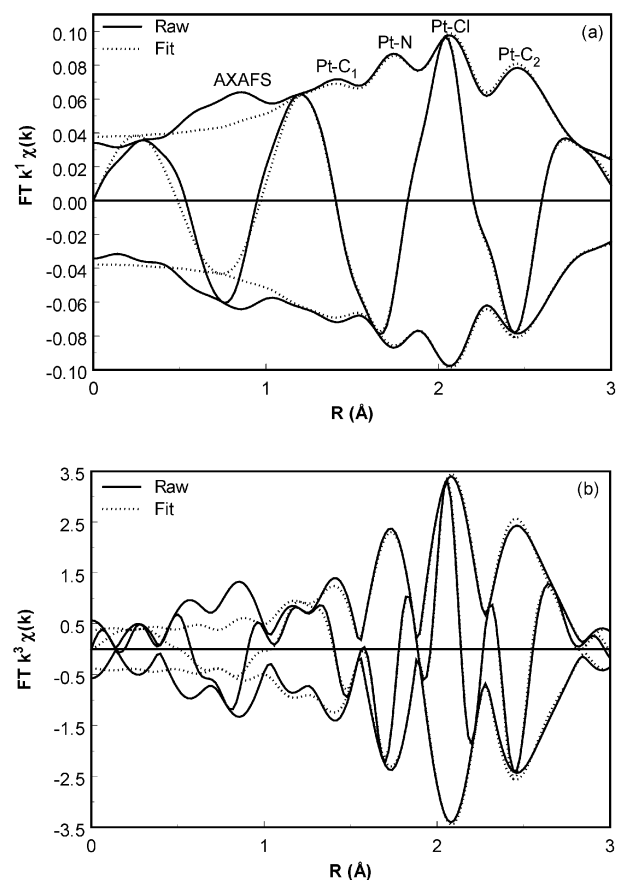

Fig. 6 (a) Raw EXAFS data (k^0-weighted) of the [PtCl(NCN-Z)] pincer complexes, for Z = NH$_2$ (solid line), Z = H (striped line), Z = COOH (dotted line). (b) Enlargement of experimental χ data to show the S/N level.

Fig. 8 Fourier Transform of the raw EXAFS data and fit (R-space fit for 1.0 < R < 3.0 Å) of the [PtCl(NCN-H)] pincer complex (a) k^1-weighted, (b) k^3-weighted.

Table 3 Selected X-ray results of [PtCl(NCN)-Z] pincer complex, and EXAFS analyses of [PtCl(NCN)-Z] pincer complexes

Ab–Sc[a]	N	R/Å	$\Delta\sigma^2/\text{Å}^2$	$\Delta E_0/\text{eV}$	Var. im.[a]	Var. abs.[a]
[PtCl-(NCN-H)] pincer complex (X-ray)						
Pt-C	1	1.907				
Pt-N	2	2.083				
Pt-Cl	1	2.407				
Pt-C	8	~2.9				
[PtCl-(NCN-NH₂)] pincer complex						
Pt-C	0.96	1.88	0.0013	−0.26	k^1-weighted:	
Pt-N	2.10	2.13	0.0002	−11.52	0.148	0.0257
Pt-Cl	1.43	2.42	0.0011	2.15	k^3-weighted:	
Pt-C	8.07	2.88	0.0054	1.90	1.04	0.475
[PtCl-(NCN-H)] pincer complex						
Pt-C	0.96	1.88	0.0016	−1.75	k^1-weighted:	
Pt-N	2.06	2.12	0.0002	−9.39	0.224	0.0673
Pt-Cl	1.41	2.43	0.0001	0.58	k^3-weighted:	
Pt-C	8.09	2.89	0.0034	0.60	0.815	0.364
[PtCl-(NCN-COOH)] pincer complex						
Pt-C	0.96	1.88	0.0009	−2.52	k^1-weighted:	
Pt-N	2.01	2.12	0.0001	−9.02	0.297	0.065
Pt-Cl	1.45	2.42	0.0006	1.05	k^3-weighted:	
Pt-C	8.09	2.89	0.0038	0.45	0.936	0.465

[a] Abbreviations: Ab = Absorber, Sc = Scatterer; Var. im. and Var. abs. are the variances in the fit of the imaginary and absolute parts, respectively. Fit: R-space, $3.0 < k < 15.0$, $1.0 < R < 3.0$.

which are in good agreement. The same is true for the k^3-weighted difference files (not shown here). Note that these isolated difference files reveal that each peak in the total FT can be attributed to a separate Pt-X neighbor, the first contribution peaking at ~1.4 Å (Fig. 8).

Fig. 9 shows that a combination of a k^1- and k^3-weighted fit is essential to obtain reliable results since anti-phase behavior is present between the different contributions.[20] Comparing the different single shell contributions, it can be observed that the Pt-C₁ and Pt-Cl contributions are in anti-phase between 1.6
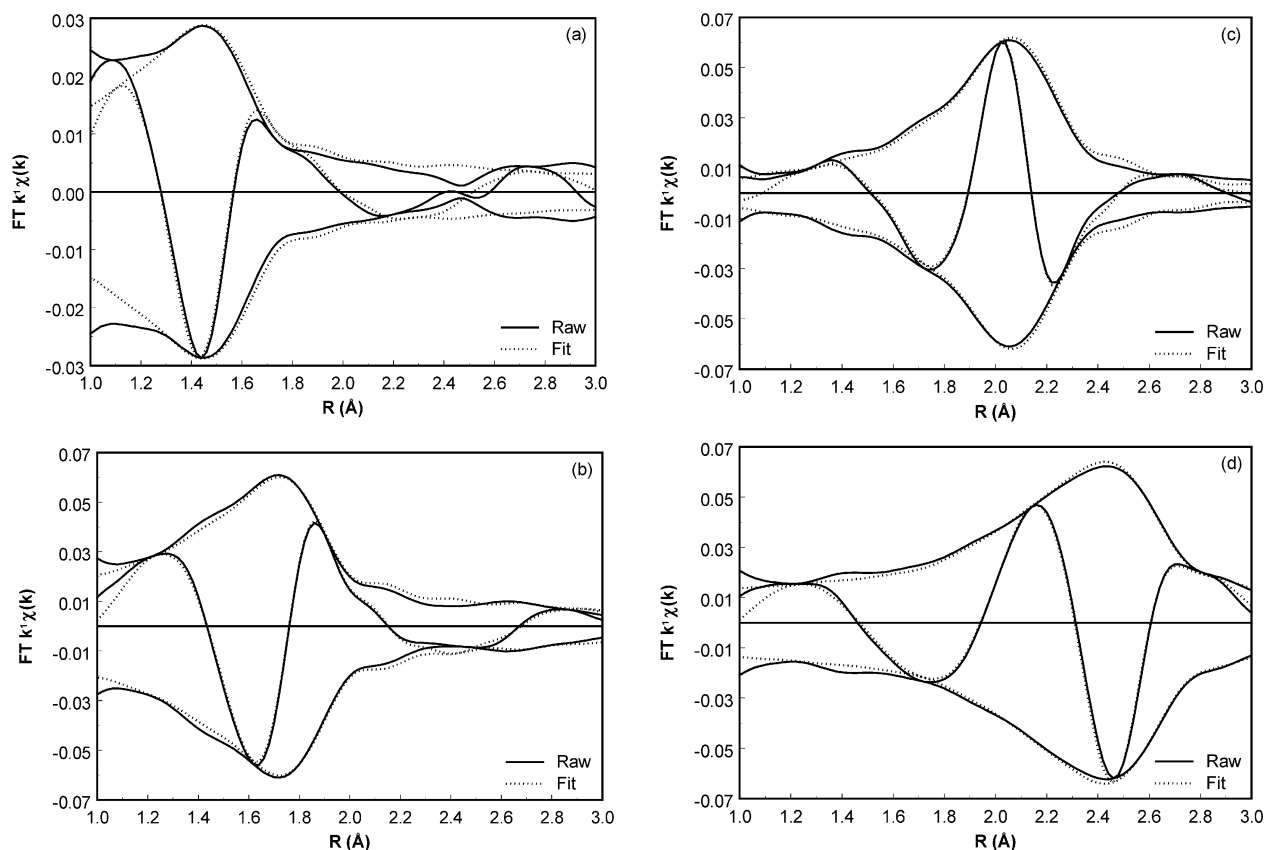

Fig. 9 Fitted single shell contributions (dotted line) and difference files (solid line) of R-space fit (k^1, $3.0 < k < 15$, $1.0 < R < 3.0$) for [PtCl(NCN-H)] (a) Pt-C₁, (b) Pt-Cl, (c) Pt-N, (d) Pt-C₂.
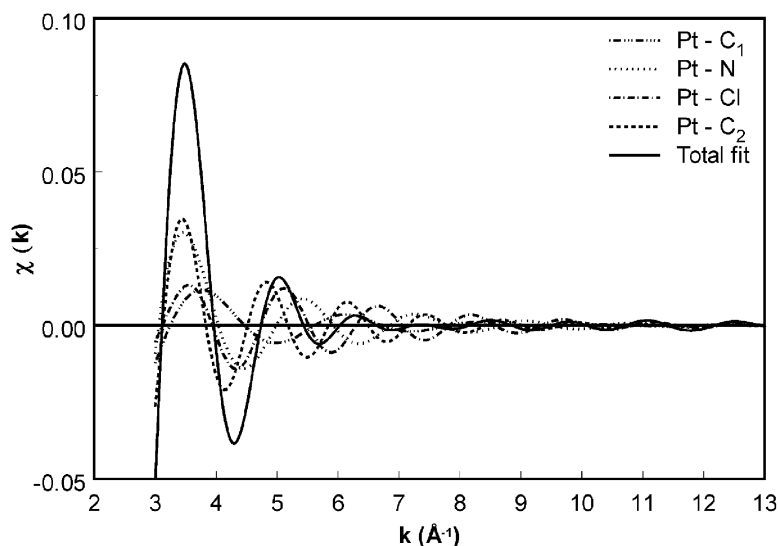
Fig. 10 χ Difference files to show anti-phase behavior between Pt-X contributions.

and 2.0 Å, whereas the Pt-N and Pt-C_2 single shell contributions are in anti-phase between 2.1 and 2.8 Å. Plotting the χ data of these single shell contributions in Fig. 10, shows that above $k = 3.5$ different contributions are in anti-phase making the total EXAFS amplitude small at high values of k. This means that a fit using only high k weightings could easily result in incorrect results. Examining the same fit with a low k-weighted FT can reveal such an incorrect fit.[20] Only if all difference files reveal a good fit in all k-weightings can a good analysis be assured. The optimal fit parameters are shown in Table 3. The single crystal X-ray results of the [PtCl-(NCN-H)] are included in Table 3 for comparison reasons (for the [PtX-(NCN-COOH)] pincer only crystal structures with X = Br, I are reported, for the [PtCl-(NCN-NH_2)] no X-ray data are available).[3] The EXAFS results of these powdered samples are shown to be consistent with the structures as established by single crystal X-ray analysis.[3] More importantly for this study, the EXAFS results for all [PtCl-(NCN-Z)] pincers are similar, *i.e.* one C atom ∼1.94 Å, two N atoms ∼2.13 Å, 1 Cl atom around 2.53 Å and 8 C atoms at a long distance with an average ∼2.9 Å.

AXAFS isolation

The AXAFS contribution is isolated from the total XAFS data by subtracting the fitted EXAFS contributions from the experimental XAFS data as shown in Fig. 11. Since the geometry around the Pt absorber is similar in all complexes, the obtained EXAFS contributions are similar (Table 3). The FT of the raw experimental EXAFS and fit for the [PtCl(NCN-H)] pincer complex is shown in Fig. 11a, along with the difference [raw EXAFS – fitted EXAFS]. This difference consists of the AXAFS contribution peaking around 0.75 Å. The small contributions at higher R are due to higher shell contributions present above 3 Å. To reveal the AXAFS contribution in comparison to the total XAFS data, the χ data of both are shown in Fig. 11b. To be able to plot only the AXAFS contribution here, without possible higher shell contributions present in the difference between raw and fitted data, these higher shells are filtered out (AXAFS shell is isolated ($3 < k < 10 \text{ Å}^{-1}, 0 < R < 1.25$ Å) and a backward Fourier transformation is performed). As can be observed in Fig. 11b, the amplitude of the AXAFS χ function is almost 50% of the total XAFS function between $4.5 < k < 8$ Å. Moreover, the AXAFS signal is significantly above the noise level (at $k = 3.18$ Å ∼40 times and at $k = 5.2$ Å even ∼1140 times).

AXAFS results

The complete background subtraction procedure is performed for all three [PtCl(NCN-Z)] pincer complexes. The absolute parts of the resulting FT's of the AXAFS data are plotted in Fig. 12a. For the [PtCl(NCN-Z)] pincer complexes with para-substituents from NH_2 to H to COOH, *i.e.* with increasing electron withdrawing properties, the AXAFS is decreasing in magnitude and its centroid is slightly shifting to lower R. Moreover, the decrease in magnitude occurs particularly between 0.75 and 1.5 Å.
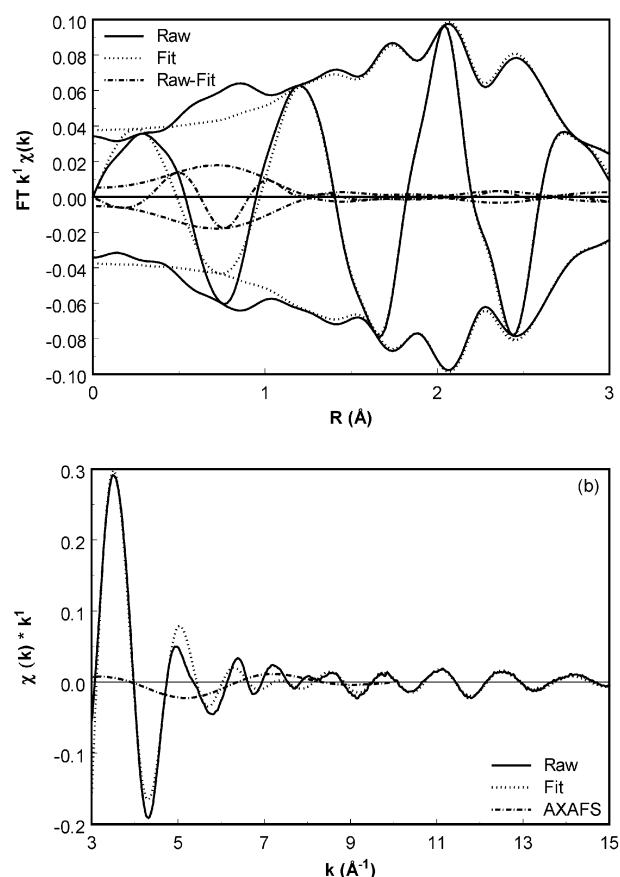

Fig. 11 Fourier Transform of the raw EXAFS data, fit (*R*-space fit for $1.0 < R < 3.0$ Å) and [Raw-Fit] for the [PtCl(NCN-H)] pincer complex (a) k^1-weighted Fourier Transform, (b) corresponding χ functions with isolated AXAFS.
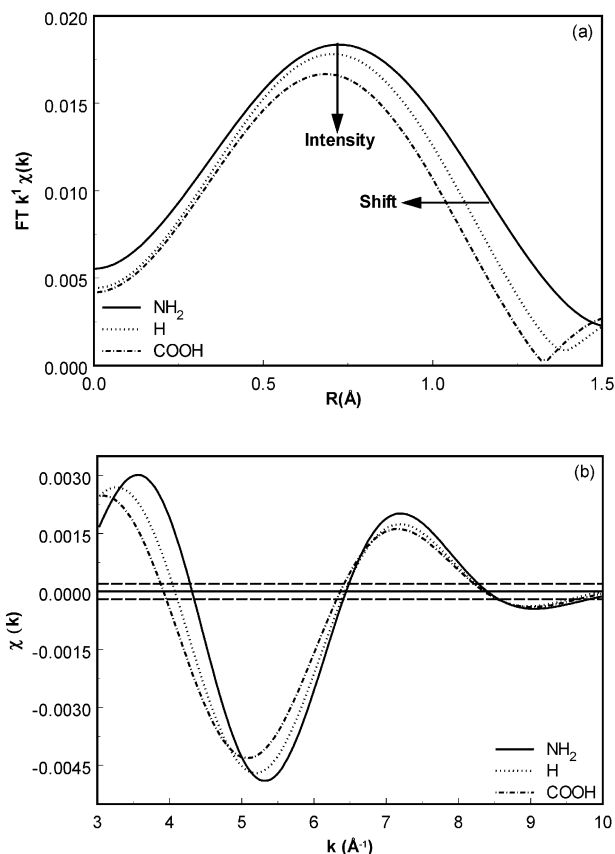
Fig. 12 (a) Fourier Transforms (k^1, $\Delta k = 3.0$–8 Å^{-1}) of AXAFS for [PtCl(NCN-NH$_2$)], [PtCl(NCN-H)] and [PtCl(NCN-COOH)] pincer complexes. The solid arrows indicate the change with increasing electronegativity. (b) Isolated AXAFS functions of the same pincer complexes.

The isolated AXAFS χ functions are displayed in Fig. 12b, including the noise level obtained. The differences between the AXAFS χ functions are significantly larger than the noise/signal level. A slight decrease in amplitude is observed when a more electron withdrawing substituent is present, consistent with the lower amplitude observed in the FT in Fig. 12a. Even more significant is the shift in k of the χ function, especially for $3 < k < 6.5$ Å^{-1}. The increase in wavelength (*i.e.* Δk between two nodes) correlates with the decrease in distance found in the FT data (Fig. 12a).

FEFF8 results

The XANES of the [PtCl(NCN-Z)] complexes can be simulated using FEFF8 and the results are shown in Fig. 13. The simulated XANES spectra clearly do not display the double peak just after the white line as was observed in the experimental spectra, neither for the L$_2$ edge nor for the L$_3$ edge, but otherwise the agreement is reasonable. The theoretical XANES spectra are the same for all three samples.

Additional FEFF8 calculations have been performed on the [PtCl(NCN-NH$_2$)] and [PtCl(NCN-COOH)] pincer complexes to simulate the different AXAFS signals as obtained in the experiment (Fig. 12). The theoretical AXAFS can be obtained from the theory either by analyzing the μ results from FEFF8 in exactly the same fashion as with the experimental data, or more directly by examining the potentials from FEFF8 used to obtain these μ results. Since the latter technique is more direct, only the potentials are shown in Fig. 14. In Fig. 14a, the different potentials U_{free}, U_{emb} and V_{int} are shown for the two complexes. The U_{emb} potentials are nearly identical for both complexes (only one line is essentially visible), and U_{free} by definition is the same, whereas the V_{int} shifts down for the
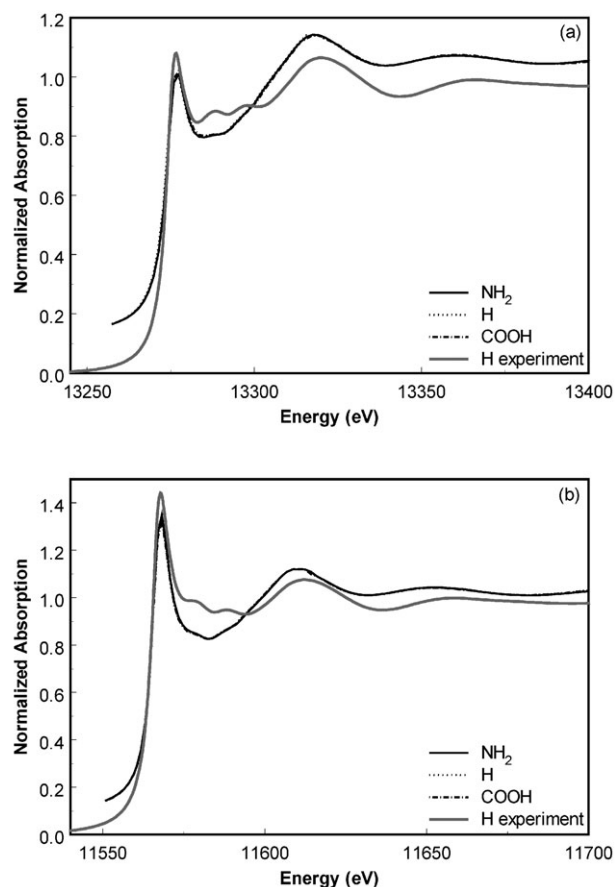
Fig. 13 Theoretical Pt XANES data for [PtCl(NCN)-Z] pincer complexes. (a) L$_2$-edge, (b) L$_3$-edge.

[PtCl(NCN-COOH)] pincer complex. The change in V_{int} shown in Fig. 14 for the two complexes is slightly larger (about 0.5 compared to 0.2 predicted by FEFF8) to better illustrate the expected changes with Z. To visualize the AXAFS contribution for the calculated complexes, the difference between the calculated potentials (equal to the AXAFS as defined above) is shown in Fig. 14b. These results show that the change in Z has no effect on the U potentials, and therefore as expected the space-field effect is negligible. Only the bond inductive effect (*i.e.* change in V_{int}) is playing a role according to FEFF8, and the change is exactly in the direction found in the experimental data (compare Fig. 12a with Fig. 14), but the change in AXAFS predicted by FEFF8 is much smaller than that found experimentally.

Discussion

The raw Pt L$_2$ and L$_3$ XANES data (Fig. 3) differ very little upon changing the *para*-substituent Z in the [PtCl(NCN-Z)] pincer complex. This is in agreement with the XANES data as calculated with FEFF8. Apparently the XANES region is not sensitive to the small electronic changes induced by the *para*-substituent of the pincer complex. The double-peak features observed in the experimental data just above the absorption edge are similar for all complexes and visible in both L-edges. Since this double peak is not simulated with FEFF8 as shown in Fig. 13, the origin of these peaks is unclear and may be caused by multiplets or shake up satellites;[23–25] interactions not included in the FEFF8 theory.

After a careful background subtraction procedure and EXAFS analysis as described above, the resulting AXAFS signals are shown in Fig. 12. The changes in the shape of the FT of the AXAFS signals is strongly suggestive of Fig. 2b. A scheme for the potentials applicable specifically for the Pt pincer
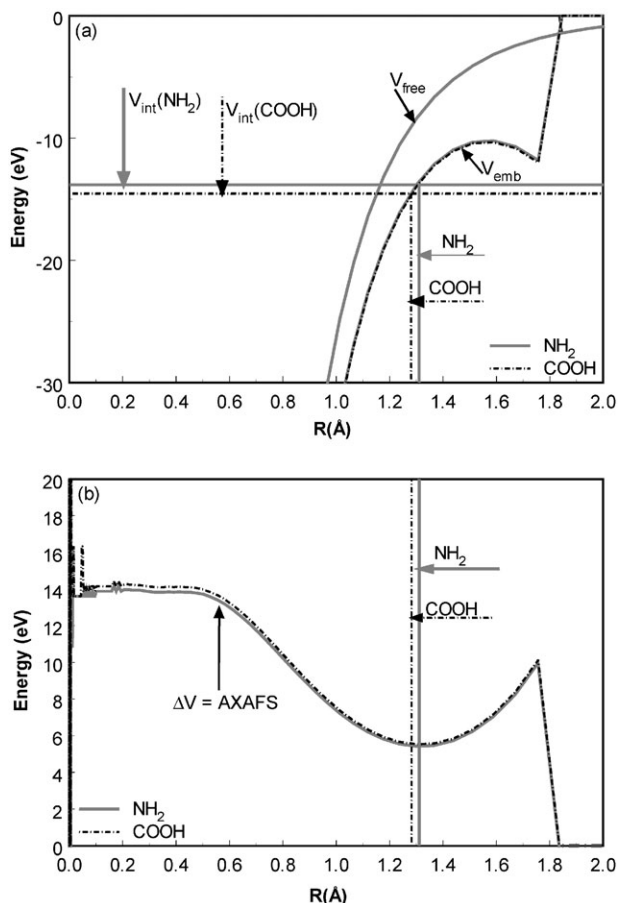
Fig. 14 FEFF8 calculated (a) potentials for [PtCl(NCN)-NH₂] and [PtCl(NCN)-COOH] pincer complexes and (b) corresponding AXAFS.

complexes is drawn in Fig. 15. It is clear that the changes in the FT of the AXAFS data reflect a downward shift in V_{int} with increasing electron-withdrawing properties of the *para*-substituent, *i.e.* the bond inductive effect is governing here. This shift in V_{int} is even more obvious in Fig. 12b, which shows a systematic shift at low k values. This is exactly what would be expected with a change in V_{int}, since V_{int} determines the effective bottom of the "conduction band" or continuum and hence the effective zero of energy E_0 in the continuum. As the zero of energy shifts, the low values of k shift, since $k \propto \sqrt{((E - E_0)^2)}$. Chemically, this downward shift in V_{int} means that the electron density near the Fermi level or HOMO on the Pt atom (Scheme 1b) is decreasing, *i.e.* the electron density on the Pt is decreasing.

FEFF8 calculations confirm that the V_{emb} potentials do not change with Z (Fig. 14a), *i.e.* that the Coulomb-field effect is negligible for these complexes. Only changes in V_{int} occur, *i.e.* the bond inductive effect is significant. Although the changes as predicted by FEFF8 are much smaller than observed in the experimental results, the identical trends in the bond inductive effect is found. The SCF muffin-tin approximation made in FEFF8 is well-known not to be fully adequate for
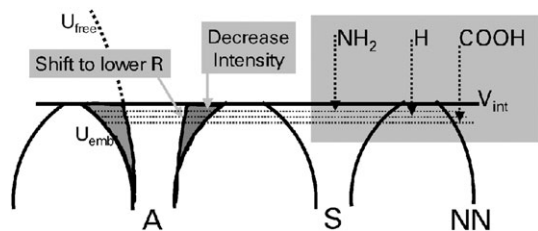

Fig. 15 Schematic potential model showing the V_{int} changes for the different [PtCl(NCN-Z)] pincer complexes.

charge-transfer (*i.e.* ionic) complexes such as those studied here. It is therefore not surprising that FEFF8 underestimates the magnitude of the inductive effect, even though it does predict the proper trends.

As discussed above, the AXAFS isolation is preceded by a very careful and systematic background procedure. Also the EXAFS analysis has to be carried out reliably. It is still possible that uncertainties occur in the final AXAFS contribution. FEFF8 results in Fig. 14 suggest that the AXAFS is significant all the way down to $R = 0$ Å. This is believed to result from the large positive valence of the Pt atom (nominally +1 or more) in these complexes, since in previous work on zero valent Pt clusters, the AXAFS was predicted to go to zero at $R = 0$ Å. Thus our background subtraction criteria, developed from analyses for zero-valent Pt clusters, automatically forced the AXAFS extracted from our experimental data to be near zero at $R = 0$ Å. This suggests that different background subtraction criteria may have to be developed for highly valent absorber atoms.

The applied background subtraction procedure thus can introduce an uncertainty in the AXAFS intensity, which increases when going to lower k and R. As already noted in the results however, the choice of a less perfect SM value (*i.e.* background) does not influence the trend in AXAFS intensity observed for these complexes, provided that a similar background subtraction procedure is applied for all complexes under investigation. Thus, quantitatively the trend in AXAFS changes is not highly dependent on the exactly correct background subtraction, even though the absolute magnitude may be. The same holds for the EXAFS analysis. Large differences in AXAFS area are observed for different EXAFS analysis results. If however consistent criteria for the EXAFS fitting procedure are applied for all samples, the observed trends are correct. In summery, the AXAFS trends for a series of complexes can be determined quite accurately although the exact quantification is much more difficult. Since consistent trends are always found, the relative precision must be better than the difference between the samples, *i.e.* 10%.

The AXAFS is defined as $[U_{emb}(R) - U_{free}(R)]$, *i.e.* the grey area in Figs. 2 and 13 as explained above. The AXAFS integrated areas are therefore obtained from the FT plots in Fig. 12a. Fig. 16 shows that a linear correlation exists between the AXAFS integrated area and the Hammett constant of the *para*-substituent (with $R^2 = 0.985$). Although the uncertainty in the AXAFS determination is rather high as described above (and see Fig. 12), a good linear correlation is obtained in Fig. 16.

A [195]Pt NMR study on these [PtCl(NCN-Z)] pincer complexes has been described in detail. NMR is shown to be a sensitive probe for the change in electron density on the metal atom (see ref. 3b). In general, an increase in electron density on the metal
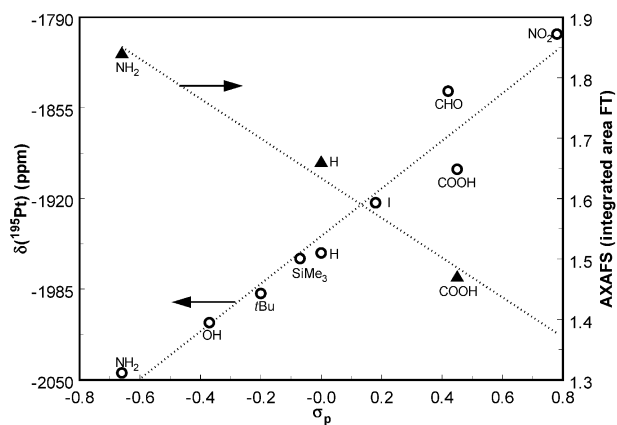

Fig. 16 [195]Pt chemical shift (empty circles) and AXAFS integrated area (filled triangles) of [PtCl(NCN-Z)] as a function of the σ_p Hammett substituent constant.

leads to an increase in shielding of the nucleus. This change in nuclear shielding is reflected in the NMR chemical shift. This shielding can be solely attributed to the *para*-substituent in the pincer systems and Fig. 16 shows a linear correlation between the Pt chemical shift and the Hammett constant of the *para*-substituent (with a correlation of $R^2 = 0.981$).[3b]

The experimental and data-analysis procedures (and the consequent reliability of the results) required for the AXAFS and NMR techniques described here are completely different. Nevertheless, the correlation between electron donating and withdrawing properties, as reflected in the Hammett constant, and the AXAFS intensity as found for these [PtCl(NCN-Z)] pincer complexes is in very good agreement with that found for the ^{195}Pt NMR data. The results obtained in this work show that AXAFS is a sufficiently sensitive probe to determine the electron density on a metal atom, similar yet complementary to NMR. The sensitivity of the XANES is observed to be too low to probe the electronic changes induced by the different substituents in this work. This has probably to do with the different energy ranges of respectively AXAFS and XANES spectroscopy. The AXAFS data is carefully extracted from the XAFS data over the range $k = 3{-}8$ Å^{-1}, whereas the XANES data only reflect the energy range up to about $k = 4$ Å^{-1} ($E < 50$ eV).

In summary, the XAFS data of the [PtCl(NCN-Z)] pincer complexes can be used to demonstrate the validity of the AXAFS technique and its intuitive description in particular. The geometry around the absorber atom remains the same (leading to the same Coulomb field effect) and only the bond inductive effect is playing a role. This facilitates the analysis and interpretation of the data.

Conclusions

We have shown that AXAFS can be used to probe the electronic properties of Pt and, in principal, of every atom, which is especially interesting for systems that, *e.g.*, are not amenable to NMR. Moreover, XAFS measurements can be performed *in situ* so the changes in electronic properties can be monitored under operating or reactive conditions and, most interestingly, even time-resolved measurements can be performed to examine changes in the catalysts with time during reaction.

The results presented in this study show that both the AXAFS and NMR techniques are sensitive to the small electronic changes induced by the *para*-substituent on [PtCl(NCN-Z)] pincer complexes, whereas the XANES technique is not. Theoretical FEFF8 calculations predict the proper trends. They are inadequate (as expected) to simulate the exact magnitude of the changes in the electronic structure with *para*-substituent. However, they do confirm for the [PtCl(NCN-Z)] pincer complexes the dominance of the bond inductive over the Coulomb-field effect and predict the same trend with the electronegativity of the substituent as observed in experiment.

Acknowledgements

References

1 (*a*) For overview articles on pincer chemistry see:M. Albrecht and G. van Koten, *Angew. Chem., Int. Ed. Engl.*, 2001, **40**, 3750; (*b*) B. Rybtchinski and D. Milstein, *Angew. Chem.*, 1999, **111**, 918; (*c*) P. Steenwinkel, R. A. Gossage and G. van Koten, *Chem. Eur. J.*, 1998, **4**, 759; (*d*) R. A. Gossage, L. A. van de Kuil and G. van Koten, *Acc. Chem. Res.*, 1998, **31**, 423; (*e*) M. H. P. Rietveld, D. M. Grove and G. van Koten, *New J. Chem.*, 1997, **21**, 751; (*f*) G. van Koten, *Pure Appl. Chem.*, 1998, **61**, 1681.

2 L. A. van der Kuil, H. Luitjes, D. M. Grove, J. W. Zwikker, J. G. M. van der Linden, A. M. Roelofsen, L. W. Jenneskens, W. Drenth and G. van Koten, *Organometallics*, 1994, **13**, 468.

3 (*a*) M. Q. Slagt, R. J. M. Klein Gebbink, M. Lutz, A. L. Spek and G. van Koten, *J. Chem. Soc., Dalton Trans.*, 2002, 2591; (*b*) M. Q. Slagt, G. Rodriguez, M. M. P. Grutters, R. J. M. Klein Gebbink, W. Klopper, M. Lutz, A. L. Spek and G. van Koten, *Chem. Eur. J.*, 2004, **10**(6), 1331.

4 D. E. Ramaker, J. de Graaf, J. A. R. van Veen and D. C. Koningsberger, *J. Catal.*, 2001, **203**(1), 7.

5 H. Wende, Ch. Litwinski, T. Gleitsmann, Z. Li, C. Sorg, K. Baberschke, A. L. Ankudinov, J. J. Rehr and Ch. Jung, *J. Phys. Condens. Matter*, 2003, **15**, 5197.

6 M. Tromp, J. A. van Bokhoven, M. Q. Slagt, R. J. M. Klein Gebbink, G. van Koten, D. E. Ramaker and D. C. Koningsberger, *J. Am. Chem. Soc.*, 2004, **126**(13), 4090.

7 F. W. H. Kampers, T. M. J. Maas, J. van Grondelle, P. Brinkgreve and D. C. Koningsberger, *Rev. Sci. Instrum.*, 1989, **60**, 2635.

8 B. W. Holland, J. B. Pendry, R. F. Pettifer and J. J. Bordas, *Physica C*, 1978, **11**, 633.

9 J. J. Rehr, C. H. Booth, F. Bridges and S. I. Zabinsky, *Phys. Rev. B*, 1994, **49**, 12347.

10 G. E. van Dorssen, D. C. Koningsberger and D. E. Ramaker, *J. Phys. Condens. Matter*, 2002, **14**, 13529, and references therein.

11 D. E. Ramaker, B. L. Mojet, W. E. O'Grady and D. C. Koningsberger, *J. Phys. Condens. Matter*, 1999, **10**, 1.

12 D. E. Ramaker, X. Qian and W. E. O'Grady, *Chem. Phys. Lett.*, 1999, **299**, 211.

13 (*a*) H. Wende and K. Baberschke, *J. Electron Spectrosc. Relat. Phenom.*, 1999, **101–103**, 821; (*b*) H. Wende, P. Srivastava, R. Chauvistre, F. May, K. Baberschke, D. Arvanitis and J. J. Rehr, *J. Phys.: Condens. Matter*, 1997, **9**, L427.

14 B. K. Teo, in *EXAFS: Basic Principles and Data-analysis*, Springer, New York, 1986.

15 D. C. Koningsberger, B. L. Mojet, G. E. van Dorssen and D. E. Ramaker, *Top. Catal.*, 2000, **10**, 143.

16 J. W. Cook, Jr. and D. E. Sayers, *J. Appl. Phys.*, 1981, **52**, 5024.

17 M. Vaarkamp, J. C. Linders and D. C. Koningsberger, *Physica B*, 1995, **208–209**, 159.

18 A. L. Ankudinov, B. Ravel, J. J. Rehr and S. D. Conradson, *Phys. Rev. B*, 1998, **7565**.

19 D. C. Koningsberger, B. L. Mojet, G. E. van Dorssen and D. E. Ramaker, *Top. Catal.*, 2000, **10**, 143.

20 M. Tromp, J. A. van Bokhoven, A. M. Arink, J. H. Bitter, G. van Koten and D. C. Koningsberger, *Chem. Eur. J.*, 2002, **8**, 5667.

21 A. L. Ankudinov, B. Ravel, J. J. Rehr and S. D. Conradson, *Phys. Rev. B*, 1998, **58**, 7565.

22 G. E. van Dorssen, D. C. Koningsberger and D. E. Ramaker, *J. Phys. Condens. Matter*, 2002, **14**, 13529.

23 F. M. F. de Groot, *J. Electron Spectrosc. Relat. Phenom.*, 1994, **67**, 529.

24 J. A. van Bokhoven, T. Nabi, H. Sambe, D. E. Ramaker and D. C. Koningsberger, *J. Phys. Condens. Matter*, 2001, **13**(45), 10247.

25 J. A. van Bokhoven, D. E. Ramaker and D. C. Koningsberger, *J. Phys. Condens. Matter*, 2001, **13**(46), 10383.